FLOW ANALYSIS OF SQUEEZE FILM DAMPERS OPERATING WITH BUBBLY LUBRICANTS

by

Dr. L. Tao
Sergio Diaz
Dr. K. Rajagopal
Dr. L. San Andrés

May 1998

TRC-SFD-2-98

Texas A&M University
Mechanical Engineering Department

FLOW ANALYSIS OF SQUEEZE FILM DAMPERS OPERATING WITH BUBBLY LUBRICANTS

Dr. L. Tao, Research Associate
S. Diaz, Graduate Student

Principal Investigators
L. San Andrés and K.R. Rajagopal

May 1998

A Research Progress Report to the
Turbomachinery Research Consortium

FLOW ANALYSIS OF SQUEEZE FILM DAMPERS OPERATING WITH BUBBLY LUBRICANTS

L. TAO, S. DIAZ, L. SAN ANDRÉS AND K.R. RAJAGOPAL

EXECUTIVE SUMMARY

Rotor-bearing systems supported in squeeze film dampers (*SFDs*) show large amplitude vibratory motions when traversing critical speeds. At these operating conditions air is drawn into the damper thin film clearance creating a bubbly mixture with the lubricant and producing SFD forces not readily predictable with currently available computational analysis. Measured film pressures and estimated damper forces provide fundamental empirical evidence for validation of a model for squeeze film bubbly flows. This year, a flow model based on the *Continuum Theory of Mixtures* describes the average motion of the squeeze film bubbly fluid using transport equations for each constituent. Empirical information from prior experimental results is used to calibrate the effective viscosity of the bubbly fluid. Computed predictions for peak-peak dynamic pressures and fluid film forces agree reasonably well with test results from a *SFD* operating with a controlled air in oil mixture. The novel bubbly flow model provides a computational tool for the improved design of squeeze film dampers with actual operating conditions.

Further experimental measurements of squeeze film pressures, forces and flow visualizations of the bubbly flow field in a *SFD* should be conducted to verify or modify some of the model assumptions. The test program should also aim to characterize the force performance of *SFDs* at high frequencies and large orbital journal motions.

FLOW ANALYSIS OF SQUEEZE FILM DAMPERS OPERATING WITH BUBBLY LUBRICANTS

L. Tao, S.Diaz, L. San Andrés and K.R. Rajagopal

TABLE OF CONTENTS

NOMENCLATURE

a	weight function for bubbly lubricant effective viscosity.
c	*SFD* nominal clearance.
C	constant.
D	rate of deformation tensor.
div	divergence operator.
e	journal orbit radius or eccentricity.
e_X, e_Y	journal eccentricity components in X and Y directions.
f_r, f_t	radial and tangential force per unit length acting at axial location z.
F_r, F_t	*SFD* radial and tangential forces.
h	$c + e\cos\theta$, film thickness.
I	identity tensor.
L	*SFD* journal length.
P	pressure of bubbly lubricant.
R	journal radius.
$\Re$	specific gas constant.
t	time.
T	temperature of bubbly lubricant.
$\mathbf{u} = (u_\theta, u_y, u_z)$	fluid velocity components in fixed coordinate system.
(x, y, z)	moving coordinate system.
(x^*, y^*, z^*)	fixed coordinate system.
$\bar{z}$	dimensionless axial coordinate.
α	volume fraction of air,
α_i	volume fraction of air at inlet of *SFD*.
ε	e/c, dimensionless orbit radius.
θ, θ^*	circumferential coordinates (moving and fixed).
$\bar{\theta}$	normalized circumferential coordinate.
μ	fluid effective viscosity.
ρ	mass density.
$\boldsymbol{\sigma}$	stress tensor.
ω	whirl frequency.
∇	gradient operation.

Subscripts

0	refers to the exit plane of *SFD*.
G	refers to gas effective properties.
GR	refers to the gas (air) material or reference properties.
I, J	refer to grid position in $\bar{\theta}$ and $\bar{z}$ directions.
L	refers to lubricant effective properties.
LR	refers to the lubricant material or reference properties.
r	refers to the radial direction.
t	refers to the tangent direction.

INTRODUCTION

Thin film bearings using lubricants and process liquids reduce friction and wear, provide load capacity and add damping to attenuate vibrations. Journal bearings represent the vast majority of applications where the mechanical surfaces shear the fluid causing it to flow and to produce the physical-wedge effect. In zones of local converging film thickness, the hydrodynamic pressure rises to a peak and then decreases to ambient values at the side and trailing edges of the thin film. In zones where the film thickness locally increases, the fluid pressure may drop to ambient or to its vapor pressure leading to the release of dissolved gases within the lubricant or lubricant vaporization. This phenomenon of film rupture, characteristic of steadily loaded bearings, is universally known as *lubricant cavitation*, vaporous or gaseous, and its effects on the performance and stability of steadily loaded bearings are reasonably well understood (Dowson, et al., 1974; Brewe, et al., 1990).

Often fluid film bearings, and most notably squeeze film dampers (*SFDs*), must support large dynamic loads, transient or periodic, which cause the fluid to go through sudden flow reversals. The fluid film pressure may fall repeatedly to ambient or to the lubricant vapor pressure if the bearing is fully submerged in a lubricant bath. However in open-ended bearings, the lubricant not only releases its gaseous content but the dynamic journal motion draws air into the film. Large amplitude journal motions at high frequencies lead to the generation of a bubbly liquid that affects the bearing dynamic forced performance. The air, entrapped within the film as bubbles, persists in the fluid film even in the zones of high dynamic pressures. Foamy oil at the damper outlet evidences this pervasive operating condition. Zeidan, et al. (1996) review the state of the art in *SFDs* and remark about the importance of the air entrainment phenomenon since it reduces considerably the dynamic fluid film bearing forces and the overall damping capability of *SFDs*. To date, however, no accurate models exist to address the effects of air ingestion on dynamically loaded journal bearings and *SFDs*. The relevant experimental measurements conducted at the TAMU Rotordynamics Laboratory could aid in validating predictive analysis (Diaz and San Andrés, 1997).

EXPERIMENTAL EVIDENCE FOR FLUID CAVITATION IN SQUEEZE FILM DAMPERS

There are two regimes of dynamic fluid cavitation in a *SFD*. The appearance of each regime depends on the damper type (sealed or open to ambient), level of supply pressure, whirl frequency, and magnitude of dynamic load producing small or large journal excursions within the film clearance.

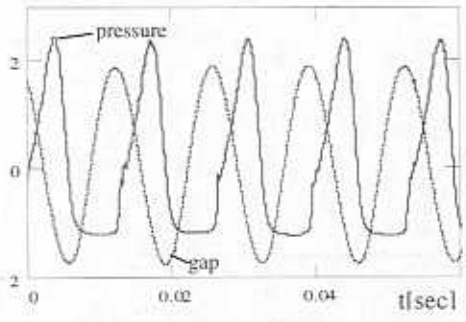

Figure 1. Dynamic film pressures (bars) and local film gap (mm x 10) in a SFD with vapor cavitation

Lubricant vapor cavitation appears in dampers with tight end seals that prevent the entrainment of external gaseous media and in operation with large supply pressures. In this last case, the through oil flow also prevents the ingestion of air. Furthermore, the lubricant must be relatively free of dissolved gases such as air, a condition not readily found in practice. Figure 1 depicts a typical measured dynamic film pressure versus time in a *SFD* operating

with oil vapor cavitation. The damper test rig is described later in this report. The test corresponds to a fully flooded condition at 1.45 bar of pressure supply, a through flow of 0.12 liters/min and 27°C film temperature. The local dynamic film gap is shown as a dashed line. The experiment illustrates the variation of pressure and gap for five periods of journal motion. The whirl frequency and centered journal orbital amplitude equal 75 Hz and 0.180 mm, respectively. The flat zone in the dynamic pressure corresponds to nearly zero absolute pressure. Note that the lubricant vapor cavity appears only during that portion of the journal motion cycle where the film gap increases. The vapor bubble collapses immediately as the local pressure raises above the oil vapor pressure. Nearly identical squeeze film pressures are reproduced for each period of journal motion. In general, correlations of measured pressures and vapor cavitation extent with predictions based on traditional film rupture models are satisfactory.

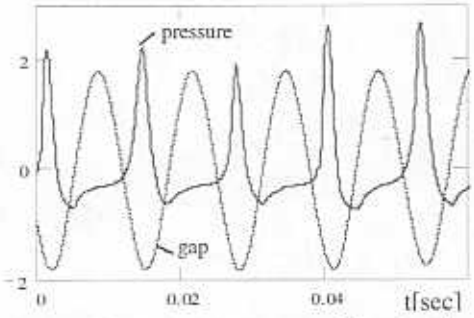

Figure 2. Dynamic film pressures (bars) and local film gap (mm x 10) in a SFD with air entrainment.

Air in oil (bubbly) fluids appear in vented dampers operating at high frequencies and with low levels of external pressurization. A suction pressure draws air into the thin film at locations where the local film gap increases. The cyclic fluid motion leads to air entrapment with bubbles remaining in the zones of dynamic pressure generation above ambient. The bubbles may shrink, break up into smaller bubbles, or diffuse within the lubricant. Figure 2 depicts the typical dynamic film pressures versus time in a damper open to ambient conditions. The operating conditions are identical as those given for the measurements depicted in Figure 1, except that the damper is not submerged in oil. The size and concentration of the ingested bubbles depend on the journal whirl frequency and amplitude. Operation at increasingly higher frequencies leads to finer more concentrated bubble distributions and the formation of a two-component foamy fluid. The dynamic pressures shown in Figure 2 reveal important differences when compared to those pressures induced by lubricant vapor cavitation (See Figure 1.) In the case of air ingestion, the squeeze film pressures differ markedly in each period of journal motion with peak pressures showing large variations. The pressure flat zone typically denoted as *gaseous cavitation* is nearly at ambient pressure. The generation of subambient film pressures is also unique at the times when the journal moves from minimum to maximum film thickness.

Childs (1993) notes that, because of cavitation phenomena, correlation between theory and an experiment is less compelling for dampers than journal bearings. The authors believe that the vast majority of *SFD*s inevitably operate with bubbly lubricants considering the low levels of pressure supply, flow rates and high operating frequencies. Of course, mixed operation regimes can also occur in practice. For instance, tightly sealed dampers may show both vapor and air entrainment type cavitation where gas bubbles may coexist around a large lubricant vapor bubble.

MEASUREMENTS OF FILM PRESSURES IN A BUBBLY FLUID *SFD*

The research at the Rotordynamics Laboratory aims to quantify the effects of controlled air in oil mixtures in the generation of dynamic film pressures in a *SFD* test rig. The experiments emulate air entrainment in an open end damper operating with a centered whirl orbit of nominal amplitude equal to 50% of the film clearance. Diaz and San Andrés (1997, 1998a,b) describe in full the test rig, experimental procedure and uncertainty, measured squeeze film pressure fields and estimated damper forces.

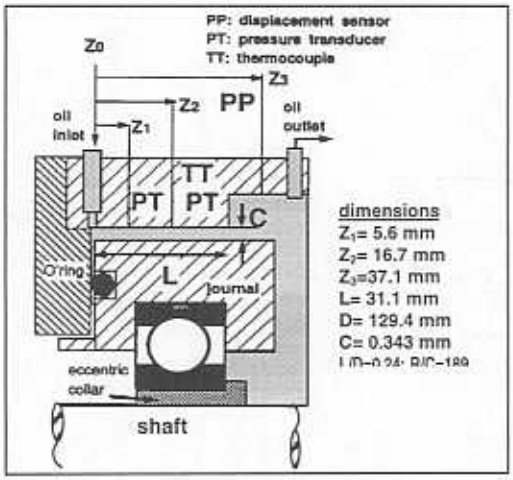

(a) Squeeze film damper detail

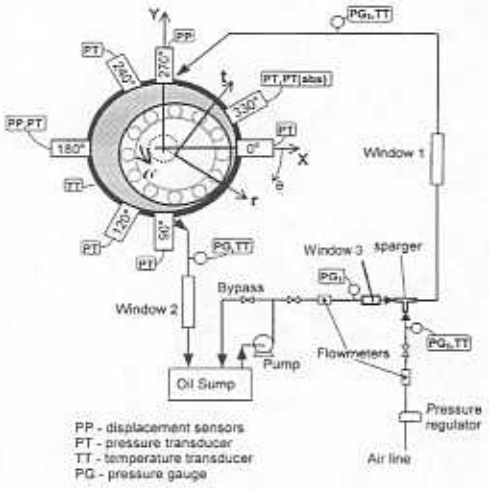

(b) Schematic of flow loop and instrumentation

Fig. 3 Squeeze film damper test rig

Figure 3 depicts the damper test section, flow loop, measuring instruments and relevant nomenclature. The damper journal diameter and axial length equal to 129.4 mm and 31.1 mm, respectively. The journal and its ball bearing are mounted eccentrically on a rigid shaft. Four anti-rotation pins prevent the journal rotation. A variable speed *DC* motor and belt transmission drive the shaft supported on two precision ball bearings. At a pressurized condition of 7.0 bar the nominal radial clearance and orbit radius are equal to 0.343 mm and 0.180 mm, respectively. The left end of the damper is tightly sealed with an O-ring, while its right end opens to an exit plenum at a uniform pressure. The lubricant enters the damper through two holes at the top (90°) and bottom (270°) of the damper left end.

Experiments are performed with an *ISO VG 68* pure lubricant of density and viscosity equal to 0.87 gr/cm^3 and 77.5 cp at 28 °C, respectively. The lubricant is delivered to the test section via a gear pump and mixed with compressed air in a sparger installed well upstream of the damper inlet ports, see Figure 3b. The air in oil mixture void or volume fraction (*VF*) is determined directly from measurements of the air mass flow rate and lubricant flow rate. Thermocouples detect the lubricant inlet and outlet, air supply and film temperatures. A photoelectric tachometer senses the shaft speed and two eddy current transducers record the journal motion. Six piezoelectric pressure sensors (*PT*) are flush mounted around the damper at two axial planes (Z_1 *and* Z_2) as depicted in Figure 3a,b.

Fourteen mixture compositions, with air volume fractions (*VF*) spanning from pure oil (*VF=0*) to all air (*VF=1*) have been tested. The air and lubricant supply pressures are kept constant at 6.8 bar to insure a uniform mixing and to avoid lubricant vaporization. The feed temperature is at room conditions (25 °C) while the exit plenum pressure

remains at 1.8 bar. A data acquisition system records the journal displacements and film pressures at two shaft speeds, 1,000 rpm (16.67 Hz) and 500 rpm (8.33 Hz). A 500 samples per second rate allows acquisition of 34 periods of journal motion at 16.67 Hz and 17 periods at 8.33 Hz.

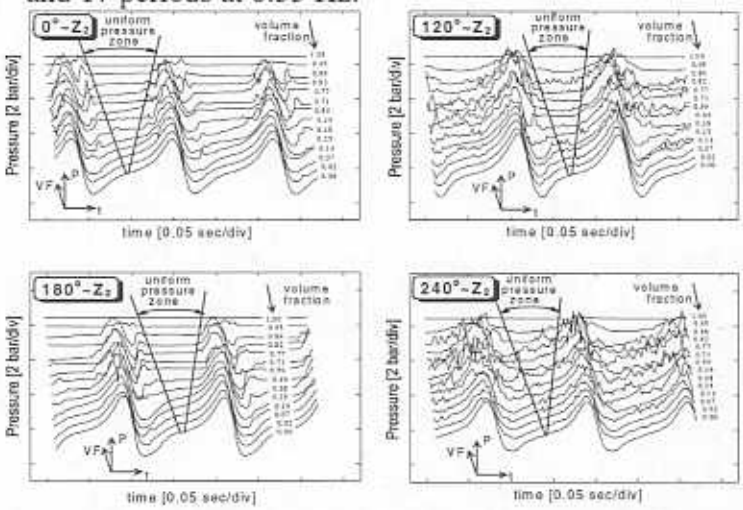

Figure 4. Development of the instantaneous pressure field and uniform pressure zone with the mixture volume fraction (VF) at different circumferential locations for a whirl frequency of 8.33 Hz

Figure 4 compiles the squeeze film pressures versus time at different circumferential positions (Z_2, θ_j). The vertical axis represents the pressure, the horizontal axis depicts the time, and the in-plane axis denotes the mixture air volume fraction (VF) varying from zero to one, i.e. the full range from pure oil to all air. The film dynamic pressures show variations from one period of journal motion to the next along with the appearance of random pressure spikes. These temporal fluctuations are nearly imperceptible for mixtures with compositions close to the pure oil condition ($VF=0$), though they increase dramatically as the air VF increases, independently of the measurement location. The sharp pressure fluctuations seem to be related to the coalescence of bubbles and/or bubbles passing in front of the pressure sensors.

A time ensemble averaging procedure results in smooth pressure fields where the high frequency "noise" is filtered. The scheme takes the entire pressure field and divides it into fields with a time period equal to that of the journal motion. Each field becomes an independent measurement and the time average of the whole ensemble is computed. The *ensemble* dynamic pressure reveals the features common to all the measured periods of the pressure field and describes the evolution of a *uniform pressure* zone also known as a *gaseous cavitation* region. Note the great similarity of the bubbly lubricant pressure profiles for large air volume fractions with those given for the air entrainment condition shown in Figure 2.

Figure 5 condenses information about the changes in peak-to-peak (p-p) film pressures as a function of the air volume fraction at the circumferential locations of measurement. The vertical bars represent the highest and lowest temporal values ever reached by the p-p pressures. In all tests, the mixtures with a very small amount of air (VF~0) produce a sharp reduction of the p-p pressures. Further increments of the air VF (from 0.02 to 0.85) cause a quasi-linear reduction on the pressures. Above a VF of 0.85, the p-p pressure drops faster, achieving a nil value for pure air. The magnitude of the temporal pressure fluctuations (vertical bars) also changes with the mixture composition. These fluctuations are just ±2% for the nearly pure oil condition, increasing to about

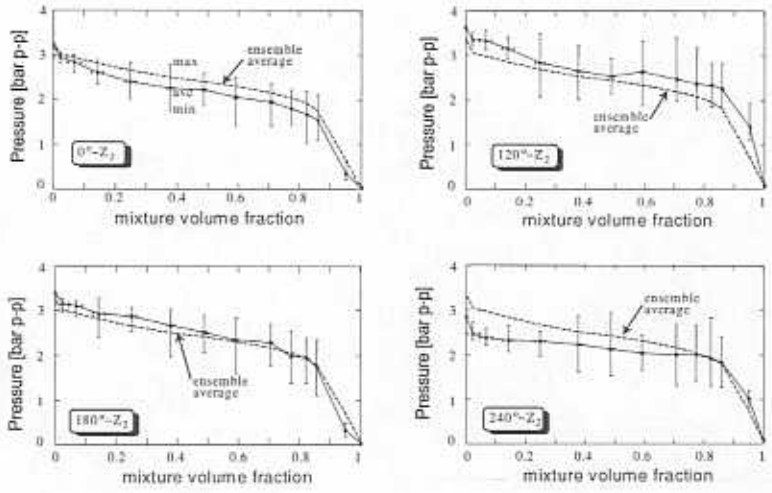

Figure 5. Peak-to-peak film pressures vs air VF at different circumferential locations of measurement (8.33 Hz)

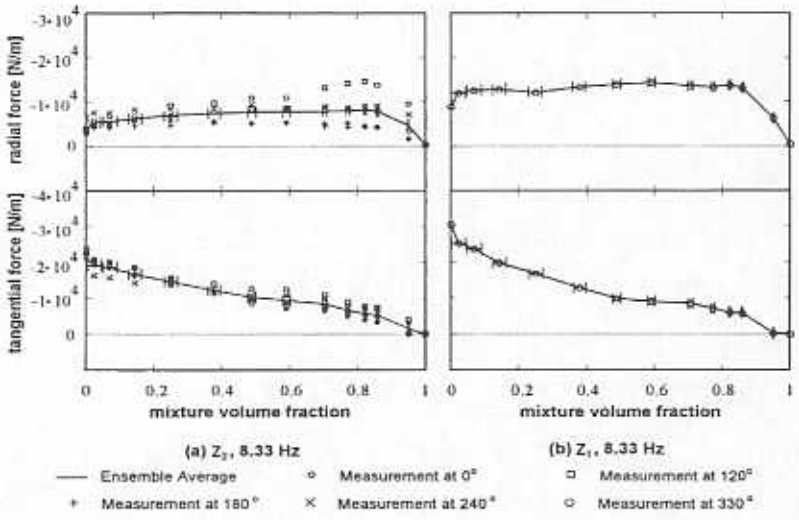

Figure 6. Dynamic film forces vs. air VF at different circumferential locations of measurement (8.33 Hz)

±45% at mixture volume fractions in the neighborhood of 0.85. Above this value, the variations drop to about ±15% for all air.

A *SFD* describing circular centered orbits and with a *stationary* pressure field generates invariant forces in a radial and tangential coordinate system rotating at the shaft speed. A tangential force ($-f_t$) is distinctive of an ideal viscous damper since it directly opposes any forward whirl motion. Radial forces (f_r) could be centering denoting a stiffness or outwards implying a virtual mass effect.

Figure 6 shows the estimated test radial ($-f_r$) and tangential ($-f_t$) forces as a function of the mixture volume fraction (*VF*). The *ensemble-averaged* forces show excellent correlation with the forces at the different angular locations of pressure measurements. The estimates of ($-f_t$) lay all within a narrow band around this *ensemble average*. The dispersion of the radial force is somewhat larger for *VF* around 0.85. The damping force ($-f_t$) presents a nearly linear variation with the air volume fraction, evidencing a reduction in the mixture effective viscosity and the overall damping capability of the *SFD*. The centering force ($-f_r$) is not affected by the mixture composition, except at the largest air volume fractions where it rapidly drops to a null value ($VF > 0.85$). However, a closer scrutiny reveals that the radial force increases rapidly from the pure oil condition to mixtures with small amounts of air ($VF < 0.02$). The radial force appears hydrostatic and related to the level of supply pressure to the test damper section.

The experimental pressure fields show fundamental differences with those arising from lubricant vapor cavitation. The tests quantify for the first time the paramount effect of the bubbly lubricant in the reduction of the dynamic force capacity of the test damper. The pervasive phenomenon of air ingestion and entrapment lacks proper physical understanding and sound analytical modeling, although relevant practice demonstrates that it greatly affects the dynamic force capability of fluid film bearing support elements. Current models for the rupture of thin films are strictly applicable to steadily loaded fluid film bearings and their extension to transient or periodic heavily loaded conditions has been successful only for bearings operating fully flooded within a lubricant bath. Prevailing analyses fail to reproduce the dynamic pressure field and forced response of vented (open ended) *SFDs* where the thin film flow field evolves into a foam-like fluid.

A NOVEL MODEL FOR *SFDs* OPERATING WITH BUBBLY LUBRICANTS

A squeeze film damper operating with a bubbly lubricant is characterized by a large number of bubbles well dispersed throughout the fluid film. The shapes and sizes of the bubbles may appear random and are certainly motion-dependent. Breakup and coalescence of bubbles may also occur. These features of the bubbly flow make impractical a Lagrangian formulation attempting to track the motion of each individual bubble. Alternately a continuum-like model for the bubbly flow within the thin film lands of a *SFD* is proposed. This model considers continuous fields of motion for both the oil and the bubbles (Bowen, 1976; Rajagopal and Tao, 1995). Note that the bubbles may be large relative to the film clearance, yet relatively small when compared to the circumference and length of a typical damper configuration. Thus, a continuum model to obtain the dynamic pressure distribution in a *SFD* appears appropriate.

Consider the physical lubricant as an incompressible Newtonian fluid with mass density ρ_{LR} and dynamic viscosity μ_{LR}. The air (ideal gas) is regarded as a compressible Newtonian fluid with dynamic viscosity μ_{GR} and its thermodynamic pressure characterized by the equation of state for a perfect gas. Further, the bubbly flow in the thin film lands of a *SFD* is assumed as isothermal and where the velocities of the lubricant and the bubbles are identical. Some experimental observations by Diaz and San Andrés (1997) appear to support this assumption which facilitates greatly the analysis.

The conservation of mass for each of the components, lubricant and air, and the balance of linear momentum for the bubbly lubricant leads to the following equations of motion (Bowen, 1976; Rajagopal and Tao, 1995):

$$\frac{\partial \rho_L}{\partial t} + \mathrm{div}(\rho_L \mathbf{u}) = 0, \tag{1}$$

$$\frac{\partial \rho_G}{\partial t} + \mathrm{div}(\rho_G \mathbf{u}) = 0, \tag{2}$$

$$\rho\left(\frac{\partial \mathbf{u}}{\partial t} + \mathbf{u}\cdot\nabla\mathbf{u}\right) = \mathrm{div}\boldsymbol{\sigma}^T, \quad \rho = \rho_L + \rho_G, \tag{3}$$

The smooth fields $\mathbf{u}$ and $\boldsymbol{\sigma}$ represent the velocity and the stress tensor of the bubbly lubricant, α the gas volume fraction, and ρ_L and ρ_G correspond to the *effective* mass densities for the lubricant and gas components, respectively. The effective density of the

lubricant (ρ_L) is defined as the mass of lubricant per unit volume of mixture, and related to its material density and the gas volume fraction by,

$$\rho_L = (1-\alpha)\rho_{LR} \tag{4}$$

Substitution of equation (4) into (1) yields

$$\frac{\partial \alpha}{\partial t} - \mathrm{div}\left[(1-\alpha)\mathbf{u}\right] = 0\,. \tag{5}$$

The objective of the analysis is to obtain an appropriate constitutive structure for the bubbly lubricant stress tensor ($\boldsymbol{\sigma}$) in terms of the material properties and the motion, i.e., α, ρ_G and $\mathbf{u}$. Following well known structures for Newtonian fluids,

$$\boldsymbol{\sigma} = -P\mathbf{I} + 2\mu\mathbf{D}, \quad \mathbf{D} \equiv \frac{1}{2}\left[\nabla\mathbf{u} + (\nabla\mathbf{u})^T\right], \tag{6}$$

with

$$P = \frac{\rho_G \Re T}{\alpha}, \tag{7}$$

$$\mu = a(\alpha)\mu_{LR} + \alpha\mu_{GR}, \quad a(\alpha) \geq 0, \quad \lim_{\alpha\to 0} a(\alpha) = 1, \quad \lim_{\alpha\to 1} a(\alpha) = 0\,. \tag{8}$$

where $\Re$ is the specific gas constant for air and T the absolute temperature of the bubbly oil. The expression for pressure P, eqn. (7), is obtained under the premise that the effect of surface tension is negligible so that the lubricant and the bubbles have identical pressures. The physical mass density of gas can be estimated through (ρ_G/α); and the pressure of the gas is calculated from the equation of state for a perfect gas. The effective viscosity μ is taken as a function of the gas volume fraction (α) with μ_{GR} and μ_{LR} as its extremes in the case of pure gas or pure oil, respectively. Physically the effective viscosity (μ) should decrease as the gas volume fraction (α) increases, and so the functional form $a(\alpha)$ is also a decreasing function. The expression for $a(\alpha)$ (or μ) has to be determined from rheological measurements which are neither readily available nor easily performed. Undaunted by this complexity, the present model attempts to calibrate the viscosity function $a(\alpha)$ by performing a curve fitting of computed pressures derived from the model to some of the test pressure measurements available (Diaz and San Andrés, 1997). The reasons for this procedure are:

(i) μ is not a material property unlike the viscosity μ_{LR} for the pure lubricant. The relation for the stress tensor σ, eqn. (6), is meaningful only in a statistical sense with the uncertainty resulting from the relatively large size of the bubbles, and μ is a statistically averaged quantity with significant deviations due to the large bubble size and their random motion;

(ii) The effect of the bubble size on the effective viscosity (μ) makes this parameter dependent on the domain geometry and the flow conditions of the *SFD* since the latter controls the bubble size. Therefore, the damper can be thought as playing the role of a viscometer.

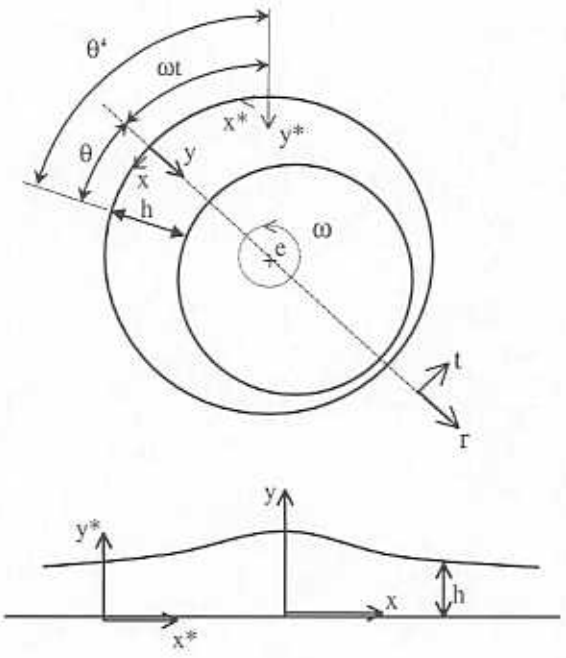

Figure 6: SFD geometry and coordinate systems for circular centered journal orbits.

Figure 6 shows the typical geometry of a *SFD* describing circular centered orbits of journal amplitude (e) at whirl frequency (ω) within a thin radial clearance (c). The fixed coordinate system (x^*, y^*, z^*) and moving coordinate system (x, y, z) are attached to the bearing with $x = x^* - \omega R t$ (San Andrés and Vance, 1986). The circumferential coordinates θ' and θ are defined by $x^* = R\theta'$ and $x = R\theta$, respectively. Let $\mathbf{u} = (u_\theta, u_y, u_z)$ be the components of the fluid velocity in the moving coordinate system where the flow appears stationary to an observer rotating with the whirl frequency (ω). The film thickness (h) in the rotating coordinate system is given by:

$$h = c + e\cos\theta, \qquad (9)$$

The equations for conservation of mass for the gas and lubricant and the momentum transport for the bubbly oil are given in the rotating coordinate frame as,

$$\frac{1}{R}\frac{\partial}{\partial\theta}(\rho_G u_\theta) + \frac{\partial}{\partial y}(\rho_G u_y) + \frac{\partial}{\partial z}(\rho_G u_z) = 0, \qquad (10)$$

$$\frac{1}{R}\frac{\partial}{\partial\theta}(\rho_L u_\theta) + \frac{\partial}{\partial y}(\rho_L u_y) + \frac{\partial}{\partial z}(\rho_L u_z) = 0, \qquad (11)$$

$$\rho\left[\frac{u_\theta}{R}\frac{\partial u_\theta}{\partial\theta} + u_y\frac{\partial u_\theta}{\partial y} + u_z\frac{\partial u_\theta}{\partial z}\right] = -\frac{1}{R}\frac{\partial P}{\partial\theta} + \frac{2}{R}\frac{\partial}{\partial\theta}\left(\frac{\mu}{R}\frac{\partial u_\theta}{\partial\theta}\right) + \frac{\partial}{\partial y}\left[\mu\left(\frac{1}{R}\frac{\partial u_y}{\partial\theta} + \frac{\partial u_\theta}{\partial y}\right)\right] + \frac{\partial}{\partial z}\left[\mu\left(\frac{1}{R}\frac{\partial u_z}{\partial\theta} + \frac{\partial u_\theta}{\partial z}\right)\right], \qquad (12)$$

$$\rho\left[\frac{u_\theta}{R}\frac{\partial u_y}{\partial\theta}+u_y\frac{\partial u_y}{\partial y}+u_z\frac{\partial u_y}{\partial z}\right]=-\frac{\partial P}{\partial y}+2\frac{\partial}{\partial y}\left(\mu\frac{\partial u_y}{\partial y}\right)$$
$$+\frac{1}{R}\frac{\partial}{\partial\theta}\left[\mu\left(\frac{1}{R}\frac{\partial u_y}{\partial\theta}+\frac{\partial u_\theta}{\partial y}\right)\right]+\frac{\partial}{\partial z}\left[\mu\left(\frac{\partial u_z}{\partial y}+\frac{\partial u_y}{\partial z}\right)\right], \qquad (13)$$

$$\rho\left[\frac{u_\theta}{R}\frac{\partial u_z}{\partial\theta}+u_y\frac{\partial u_z}{\partial y}+u_z\frac{\partial u_z}{\partial z}\right]=-\frac{\partial P}{\partial z}+2\frac{\partial}{\partial z}\left(\mu\frac{\partial u_z}{\partial z}\right)$$
$$+\frac{1}{R}\frac{\partial}{\partial\theta}\left[\mu\left(\frac{1}{R}\frac{\partial u_z}{\partial\theta}+\frac{\partial u_\theta}{\partial z}\right)\right]+\frac{\partial}{\partial y}\left[\mu\left(\frac{\partial u_z}{\partial y}+\frac{\partial u_y}{\partial z}\right)\right], \qquad (14)$$

Along with the following boundary conditions:

(i) Non-slip condition at the bearing and journal surfaces, i.e.,

$$\mathbf{u}=(-\omega R,0,0), \quad \text{at } y=0, \qquad (15)$$

$$\mathbf{u}=(-\omega R,\omega e\sin\theta,0), \quad \text{at } y=h\equiv c+e\cos\theta; \qquad (16)$$

(ii) Periodicity of the flow field in the circumferential direction (θ),

$$(\alpha,\rho_G,\mathbf{u})(\theta+2\pi,y,z)=(\alpha,\rho_G,\mathbf{u})(\theta,y,z); \qquad (17)$$

(iii) For a symmetric *SFD* with both ends open to ambient conditions,

$$\frac{\partial\alpha}{\partial z}=\frac{\partial\rho_G}{\partial z}=0, \quad \text{at } z=0, \text{ by symmetry,} \qquad (18)$$

and

$$\alpha=\alpha_0, \quad P=P_0, \quad \text{at } z=\pm L, \text{ at the exit ends,} \qquad (19)$$

where α_0 and P_0 denote the exit gas volume fraction and pressure at the damper sides. At present, these values are extracted from the detailed experiments of Diaz and San Andrés (1997). Note that in actuality the discharge gas volume fraction is determined by the damper operating conditions, which include the orbit radius and whirl frequency.

Non-dimensional variables are introduced as,

$$\bar\theta=\frac{\theta}{2\pi}, \quad \bar y=\frac{y}{c}, \quad \bar z=\frac{z}{L}, \quad \bar h=\frac{h}{c}, \quad \bar\mu=\frac{\mu}{\mu_{LR}},$$
$$\bar\rho_G=\frac{\rho_G\Re T}{P_0}, \quad \bar P=\frac{P}{P_0}, \quad \bar u_\theta=\frac{u_\theta}{\omega R}, \quad \bar u_y=\frac{u_y}{\omega c}, \quad \bar u_z=\frac{u_z}{\omega R}, \qquad (20)$$

The model follows the assumptions of classical lubrication theory, i.e. it considers the effects of fluid inertia to be negligible, and furthermore, the smallness of the clearance to radius ratio, c/R << 1, leads to a pressure field invariant across the film thickness (h). The classical model then regards the flow motion as a quasi-static equilibrium of pressure forces and the cross-film shear forces induced by the whirling motion. Note that this is essentially the standard procedure used to derive the classical Reynolds equation, see *Appendix A* for further details. The governing equations for the squeeze film bubbly flow based on the assumptions described above are:

$$(\alpha, \overline{\rho}_G, \overline{P}) = (\alpha, \overline{\rho}_G, \overline{P})(\theta, \overline{z}), \tag{21}$$

$$\frac{\partial}{\partial\theta}(\overline{\rho}_G \overline{u}_\theta) + \frac{\partial}{\partial\overline{y}}(\overline{\rho}_G \overline{u}_y) + \frac{R}{L}\frac{\partial}{\partial\overline{z}}(\overline{\rho}_G \overline{u}_z) = 0, \tag{22}$$

$$\frac{\partial}{\partial\theta}((1-\alpha)\overline{u}_\theta) + \frac{\partial}{\partial\overline{y}}((1-\alpha)\overline{u}_y) + \frac{R}{L}\frac{\partial}{\partial\overline{z}}((1-\alpha)\overline{u}_z) = 0, \tag{23}$$

$$\frac{\partial}{\partial\overline{y}}\left(\overline{\mu}\frac{\partial\overline{u}_\theta}{\partial\overline{y}}\right) = \frac{P_0}{\omega\mu_{LR}}\left(\frac{c}{R}\right)^2\frac{\partial\overline{P}}{\partial\theta}, \tag{24}$$

$$\frac{\partial}{\partial\overline{y}}\left(\overline{\mu}\frac{\partial\overline{u}_\theta}{\partial\overline{y}}\right) = \frac{P_0}{\omega\mu_{LR}}\frac{R}{L}\left(\frac{c}{R}\right)^2\frac{\partial\overline{P}}{\partial\overline{z}}, \tag{25}$$

along with

$$\overline{\mathbf{u}} = (-1,0,0), \quad \text{at } \overline{y} = 0, \tag{26}$$

$$\overline{\mathbf{u}} = (-1, \varepsilon\sin\theta, 0), \quad \text{at } \overline{y} = \overline{h} \equiv 1 + \varepsilon\cos\theta, \quad \varepsilon \equiv \frac{e}{c}, \tag{27}$$

$$(\alpha, \overline{\rho}_G)(\theta + 2\pi, \overline{z}) = (\alpha, \overline{\rho}_G)(\theta, \overline{z}), \tag{28}$$

$$\frac{\partial\alpha}{\partial\overline{z}} = \frac{\partial\overline{\rho}_G}{\partial\overline{z}} = 0, \quad \text{at } \overline{z} = 0, \tag{29}$$

$$\alpha = \alpha_0, \quad \overline{P} = 1, \quad \text{at } \overline{z} = 1. \tag{30}$$

Direct integration of the momentum equations (24) and (25) and application of the non-slip boundary conditions, equations (26-27), leads to

$$\overline{u}_\theta \equiv \tilde{u}_\theta - 1 = \frac{P_0}{2\omega\mu_{LR}}\left(\frac{c}{R}\right)^2\frac{1}{\overline{\mu}}\frac{\partial\overline{P}}{\partial\theta}\overline{y}(\overline{h} - \overline{y}) - 1, \tag{31}$$

$$\bar{u}_z = \frac{P_0}{2\omega\mu_{LR}}\frac{R}{L}\left(\frac{c}{R}\right)^2\frac{1}{\bar{\mu}}\frac{\partial\bar{P}}{\partial\bar{z}}\bar{y}\left(\bar{h}-\bar{y}\right). \tag{32}$$

Here $\bar{u}_\theta$ represents the circumferential fluid velocity in the fixed coordinate system. Note that the bubbly fluid velocities are a result of hydrodynamic pressure gradients, i.e. a pure Poiseuille type flow. Further, integration of the mass conservation eqns. (22) and (23) across the film, $\bar{y}$-direction, and applying eqns. (26) and (27) yields,

$$\frac{\partial}{\partial\theta}\left(\bar{\rho}_G\int_0^{\bar{h}}\bar{u}_\theta\,d\bar{y}\right)+\frac{R}{L}\frac{\partial}{\partial\bar{z}}\left(\bar{\rho}_G\int_0^{\bar{h}}\bar{u}_z\,d\bar{y}\right)=\frac{\partial}{\partial\theta}\left(\bar{\rho}_G\bar{h}\right), \tag{33}$$

$$\frac{\partial}{\partial\theta}\left((1-\alpha)\int_0^{\bar{h}}\bar{u}_\theta\,d\bar{y}\right)+\frac{R}{L}\frac{\partial}{\partial\bar{z}}\left((1-\alpha)\int_0^{\bar{h}}\bar{u}_z\,d\bar{y}\right)=\frac{\partial}{\partial\theta}\left((1-\alpha)\bar{h}\right), \tag{34}$$

Substitution of the fluid velocities, eqns. (31) and (32) with $\bar{\theta}$ used instead of θ, in the mass conservation equations (33) and (34) gives,

$$\frac{P_0}{12\omega\mu_{LR}}\left(\frac{c}{R}\right)^2\left[\frac{\partial}{\partial\bar{\theta}}\left(\frac{(1-\alpha)\bar{h}^3}{\bar{\mu}}\frac{\partial\bar{P}}{\partial\bar{\theta}}\right)+\left(\frac{2\pi R}{L}\right)^2\frac{\partial}{\partial\bar{z}}\left(\frac{(1-\alpha)\bar{h}^3}{\bar{\mu}}\frac{\partial\bar{P}}{\partial\bar{z}}\right)\right]$$
$$=\frac{\partial}{\partial\bar{\theta}}\left[2\pi(1-\alpha)\bar{h}\right]. \tag{35}$$

This equation can be cast in the familiar form of a Reynolds equation as follows,

$$\frac{1}{R^2}\frac{\partial}{\partial\theta}\left(\frac{\rho_L h^3}{12\mu}\frac{\partial P}{\partial\theta}\right)+\frac{\partial}{\partial z}\left(\frac{\rho_L h^3}{12\mu}\frac{\partial P}{\partial z}\right)=\frac{\partial}{\partial\theta}\left(\rho_L h\right).$$

where from equations (4) and (7), $\rho_L = (1-\alpha)\rho_{LR}$, $\mu = a(\alpha)\mu_{LR}+\alpha\mu_{GR}$, and $P=\dfrac{\rho_G\Re T}{\alpha}$.

Equations (33) and (34) represent the conservation of mass for the gas and lubricant components of the bubbly lubricant, respectively. Note that the current model precludes lubricant vapor cavitation or the release of dissolved gases. From equations (33) and (34) it is easily inferred that

$$\left(-\bar{h}\frac{\partial}{\partial\theta}+\int_0^{\bar{h}}\bar{u}_\theta\,d\bar{y}\frac{\partial}{\partial\theta}+\frac{R}{L}\int_0^{\bar{h}}\bar{u}_z\,d\bar{y}\frac{\partial}{\partial\bar{z}}\right)\left(\frac{\bar{\rho}_G}{1-\alpha}\right)=0, \tag{36}$$

i.e.,
$$\bar{\rho}_G = C(1-\alpha)=\frac{\alpha_0}{1-\alpha_0}(1-\alpha), \tag{37}$$

or written, with the aid of equations (4) and (20), in the form of

$$\frac{\rho_G}{\rho_L} = \frac{P_0}{\rho_{LR}\Re T}\frac{\alpha_0}{1-\alpha_0}, \tag{38}$$

which implies that the ratio between the (effective) mass density of air and the (effective) mass density of oil remains invariant throughout the bubbly flow. This equation just represents the conservation of mass principle and provides a direct relationship between the gas volume fraction and the bubbly fluid pressure, i.e. substitution of eqns. (7) and (20) above render,

$$\frac{\alpha}{\alpha_0} = \left[\alpha_0 + (1-\alpha_0)\frac{P}{P_0}\right]^{-1}, \tag{39}$$

Combining eqn. (39) with eqns. (8) and (20) yields

$$\alpha = \frac{C}{C+\overline{P}}, \quad \overline{\mu} = a(\alpha) + \frac{\mu_{GR}}{\mu_{LR}}\alpha. \tag{40}$$

Equation (35) then provides the governing equation for the mean pressure field P in the two-dimensional domain $(\overline{\theta},\overline{z}) \in [0,1]\times[0,1]$ along with the following boundary conditions from equations (28) to (30),

$$\overline{P}(0,\overline{z}) = \overline{P}(1,\overline{z}), \quad \frac{\partial}{\partial\overline{\theta}}\overline{P}(\overline{\theta},\overline{z})\Big|_{\overline{\theta}=0} = \frac{\partial}{\partial\overline{\theta}}\overline{P}(\overline{\theta},\overline{z})\Big|_{\overline{\theta}=1}, \tag{41}$$

$$\frac{\partial}{\partial\overline{z}}\overline{P}(\overline{\theta},\overline{z})\Big|_{\overline{z}=0} = 0, \quad \overline{P}(\overline{\theta},1) = 1. \tag{42}$$

NUMERICAL ALGORITHM OF SOLUTION

A finite difference procedure is used for discretization of the governing eqn. (35) on the finite region depicted in Figure 7. The dimensionless flow domain $(\overline{\theta},\overline{z}) \in [0,1]\times[0,1]$ is divided into a sequence of discrete grid points

$$(\overline{\theta},\overline{z})_{I,J} = (\overline{\theta}_I,\overline{z}_J), I = 1,2,...,M;\ J = 1,2,...,N, \tag{43}$$

Equation (35) is integrated on the square shaded area around the pressure node (I,J). The first order partial derivatives are discretized with the well known central difference formulae to obtain equations for

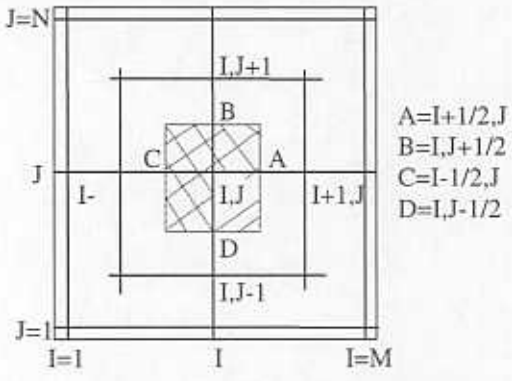

Figure 7: Discretization of flow domain for numerical procedure

the discrete pressure $P_{I,J}$ at $(IJ)\in\{2,...,M-1\}\times\{2,...,N-1\}$, i.e.

$$\left[\frac{E_{I+1/2,J}}{\overline{\theta}_{I+1}-\overline{\theta}_{I}}+\frac{E_{I-1/2,J}}{\overline{\theta}_{I}-\overline{\theta}_{I-1}}+\left(\frac{2\pi R}{L}\right)^2\frac{\overline{\theta}_{I+1}-\overline{\theta}_{I-1}}{\overline{z}_{J+1}-\overline{z}_{J-1}}\left(\frac{E_{I,J+1/2}}{\overline{z}_{J+1}-\overline{z}_{J}}+\frac{E_{I,J-1/2}}{\overline{z}_{J}-\overline{z}_{J-1}}\right)\right]P_{I,J}$$
$$=\frac{E_{I+1/2,J}}{\overline{\theta}_{I+1}-\overline{\theta}_{I}}P_{I+1,J}+\frac{E_{I-1/2,J}}{\overline{\theta}_{I}-\overline{\theta}_{I-1}}P_{I-1,J}$$
$$+\left(\frac{2\pi R}{L}\right)^2\frac{\overline{\theta}_{I+1}-\overline{\theta}_{I-1}}{\overline{z}_{I+1}-\overline{z}_{I-1}}\left(\frac{E_{I,J+1/2}}{\overline{z}_{J+1}-\overline{z}_{J}}P_{I,J+1}+\frac{E_{I,J-1/2}}{\overline{z}_{J}-\overline{z}_{J-1}}P_{I,J-1}\right)$$
$$+D_2\left\{\left[(1-\alpha)\overline{h}\right]_{I+\frac{1}{2},J}-\left[(1-\alpha)\overline{h}\right]_{I-\frac{1}{2},J}\right\}, \tag{44}$$

where

$$E(\overline{\theta},\overline{P})\equiv\frac{(1-\alpha)\overline{h}^3}{\overline{\mu}},\quad D_2\equiv\frac{24\pi\omega\mu_{LR}}{P_0}\left(\frac{R}{c}\right)^2, \tag{45}$$

$$E_{I\pm1/2,J}=E\left(\frac{\overline{\theta}_{I\pm1}+\overline{\theta}_{I}}{2},\frac{\overline{P}_{I\pm1,J}+\overline{P}_{I,J}}{2}\right),\quad E_{I,J\pm1/2}=E\left(\overline{\theta}_{I},\frac{\overline{P}_{I,J}+\overline{P}_{I,J\pm1}}{2}\right), \tag{46}$$

$$\left[(1-\alpha)\overline{h}\right]_{I\pm\frac{1}{2},J}=\left\{1-\frac{1}{2}\left[\alpha(\overline{P}_{I\pm1,J})+\alpha(\overline{P}_{I,J})\right]\right\}\overline{h}\left(\frac{\overline{\theta}_{I\pm1}+\overline{\theta}_{I}}{2}\right). \tag{47}$$

The boundary condition, eqn. (41), results for $J=2,...,N-1$, in

$$\overline{P}_{I,J}=\overline{P}_{M,J}=\frac{\overline{\theta}_{M}-\overline{\theta}_{M-1}}{\overline{\theta}_{M}-\overline{\theta}_{M-1}+\overline{\theta}_{2}-\overline{\theta}_{1}}\left(\overline{P}_{2,J}+\frac{\overline{\theta}_{2}-\overline{\theta}_{1}}{\overline{\theta}_{M}-\overline{\theta}_{M-1}}\overline{P}_{M-1,J}\right) \tag{48}$$

which results from the periodicity condition

$$\frac{\overline{P}_{2,J}-\overline{P}_{1,J}}{\overline{\theta}_{2}-\overline{\theta}_{1}}=\frac{\overline{P}_{M,J}-\overline{P}_{M-1,J}}{\overline{\theta}_{M}-\overline{\theta}_{M-1}},$$

Application of the symmetry and exit boundary conditions for the gas volume fraction, for $I=1,...,M$, leads to

$$\alpha_{1,J}=\alpha_{1,2},\quad \alpha_{I,N}=\alpha_{0}. \tag{49}$$

The numerical solution for the grip pressures $\overline{P}_{I,J}$ on $\{1,...,M\}\times\{1,...,N\}$ proceeds iteratively using eqn. (44) together with eqns. (48) and (49). The iterative scheme is described as follows:

(a) Guess an initial pressure field at the first iteration, $\overline{P}_{I,J}^{(0)}$ to $\overline{P}_{I,J}$, $(I = 1,...,M;\ J = 1,..,N-1)$, for example, take $\overline{P}_{I,J}^{(0)} = 1$ (or $\alpha_{I,J}^{(0)} = \alpha_0$);

(b) For a fixed $(\hat{I},\hat{J})$ in $\{2,...,M-1\}\times\{2,..,N-1\}$, determine $\overline{P}_{\hat{I},\hat{J}}$ from equation (44) by calculating all the terms based on $\overline{P}_{I,J}^{(0)}$, except the quantity $\overline{P}_{\hat{I},\hat{J}}$; Then, calculate $\overline{P}_{1,J}$, $\overline{P}_{I,J}$ and $\overline{P}_{M,J}$ from equations (48) and (49). This procedure results in $\overline{P}_{I,J}$, $(I = 1,...,M;\ J = 1,..,N-1)$;

(c) Check the difference between the current and prior fields, $\overline{P}_{I,J}$ and $\overline{P}_{I,J}^{(0)}$, according to $(\overline{P}_{I,J} - \overline{P}_{I,J}^{(0)})/\overline{P}_{I,J}$ $(I = 1,...,M;\ J = 1,..,N-1)$. If the difference is larger than a specified tolerance then consider $\overline{P}_{I,J}$ as an initial field $\overline{P}_{I,J}^{(0)}$, and repeat steps (a) thru (c) until a specified criteria is satisfied. An under relaxation scheme could be implemented to smooth out convergence.

Fluid film forces are calculated by integration of the calculated pressure field around the journal force. Radial and tangential forces (per unit length) at an axial location (z) are given by,

$$\begin{Bmatrix} f_r \\ f_t \end{Bmatrix} = \int_0^{2\pi} P \begin{Bmatrix} \cos\theta \\ \sin\theta \end{Bmatrix} R d\theta \,, \tag{51}$$

while the *SFD* radial and tangential forces are given by,

$$\begin{Bmatrix} F_r \\ F_t \end{Bmatrix} = \int_0^{L}\int_0^{2\pi} P \begin{Bmatrix} \cos\theta \\ \sin\theta \end{Bmatrix} R d\theta dz \,. \tag{52}$$

A computational Fortran program has been developed based on the above point-by-point iteration scheme. The parameter values used in the validation of the program are listed in Table 1 and denote the geometrical characteristics and operating conditions of the *SFD* tested by Diaz and San Andrés (1997). The values for the exit gas volume fraction (α_0), discharge pressure (P_0), film temperature (T) and journal orbit radius (e) have been obtained directly from the experimental measurements. These values are presented in Table 2 for each test condition at a whirl frequency of 8.166 Hz (ω=52.35 rad/s).

Table 1: Test squeeze film damper parameters

$\Re = 287\ \mathrm{N\cdot m/kg\cdot K}$, ω=52.35 rad/s (500 rpm), $\mu_{GR} = 1.837\times10^{-5}\ \mathrm{kg/m\cdot sec}$,
$\mu_{LR} = 1.3337\times10^{-8}\exp(4699/T)\ \mathrm{kg/m\cdot sec} \sim 96$ centipoise,
$c = 3.43\times10^{-4}$ m, $R = 6.47\times10^{-2}$ m, $L = 3.11\times10^{-2}$ m.

based on *SFD* test configuration of Diaz and San Andrés (1997)

Table 2: Bubbly flow test conditions

Test case #	α_0	α_1	P_0 (bar)	T(K)	$e_X \times 10^4$ (m)	$e_Y \times 10^4$ (m)
2	0.114	0.023	1.612	297.59	1.77	1.51
3	0.278	0.067	1.646	297.59	1.77	1.49
4	0.46	0.141	1.715	298.15	1.77	1.48
5	0.622	0.247	1.749	298.15	1.78	1.49
6	0.749	0.376	1.783	298.15	1.78	1.48
7	0.823	0.486	1.817	298.15	1.78	1.46
8	0.874	0.591	1.851	298.71	1.79	1.48
9	0.919	0.706	1.885	298.71	1.79	1.46
10	0.941	0.773	1.885	298.71	1.78	1.46
11	0.954	0.823	1.953	299.26	1.78	1.44
12	0.963	0.858	2.021	299.26	1.78	1.45
13	0.987	0.95	2.089	299.26	1.83	1.41

α_1 represents the supply or feed gas volume fraction. An average value of journal eccentricity, $e = (e_X + e_Y)/2$, is used for the numerical predictions.

Several formulas for the viscosity relationship, $a(\alpha)$, under the constraint of equation (8), have been tried to predict the dynamic film pressure field P and the peak-to-peak pressure at the axial position $z_2 = 16.6\text{mm}$ where measurements are available. Initial numerical computations reveal that an effective viscosity given by the linear relationship, $a(\alpha) = 1 - \alpha$, do not yield results compatible with the experimental measurements. After several trials it is found that the relationship,

$$a(\alpha) = (1 - \alpha^4)^{0.5} \tag{50}$$

renders numerical results which provide a better correlation with the peak-to-peak pressure measurements. The reason may be due to that this relation is relatively insensitive to the volume fraction of air (α) when this is small, and so is the effective viscosity μ, as it is clearly depicted in Figure 8 for the two correlations $a(\alpha) = 1 - \alpha$ and $a(\alpha) = (1 - \alpha^4)^{0.5}$.

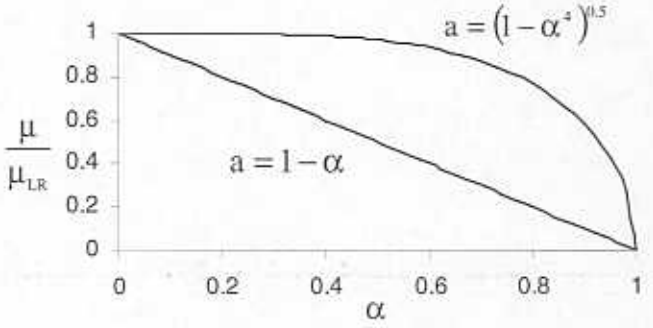

Figure 8: Relationships for the effective fluid viscosity versus the gas volume fraction (α).

The convergence criterion used in the numerical calculation is set to $\left(\overline{P}_{i,j} - \overline{P}_{i,j}^{(0)}\right)/\overline{P}_{i,j} \le 10^{-5}$. The number of grid points M and N may vary and the grids used distribute non-uniformly with finer partitions in the regions around $\overline{\theta} = 0.5$ ($\theta=\pi$) and $\overline{z} = 1$ since the test measurements and the preliminary computational show that the pressure changes rather rapidly in these regions. Values of $M = N = 76$ have been chosen to balance the conflicting demands of accuracy and computing time. In addition, further computations demonstrate that a finer mesh with $M = N = 151$ increases the computing time tremendously, though it may increase the accuracy of the numerical solution to several percent. For instance, for test case #4, see Table 2, $M = N = 76$ leads to peak-to-peak pressures at $z_1 = 5.6$mm and $z_2 = 16.7$mm equal to 2.88 and 2.18 bar, respectively, and with a computing time of 14 minutes in a Pentium PC. However, the finer grid $M = N = 151$, renders peak-to-peak pressures equal to 2.79 and 2.11 bar at the expense of a computing time equal to 150 minutes.

Numerical Predictions and Comparison to Experimental Results

Diaz and San Andrés (1997) report an experimental investigation aimed to measure the dynamic force performance of an oil lubricated *SFD* operating with air ingestion. Tests are conducted in a constrained circular orbit, open end *SFD* supplied with a controlled bubbly mixture of air and oil (see Figure 3). Detailed measurements of the *dynamic* squeeze film pressures and journal motion, film temperatures, electrical power, air and lubricant flow rates are performed at two whirl frequencies (8.33 and 16.67 Hz) as the air volume content in the bubbly lubricant increases from 0% to 100%. The analysis of *period-averaged dynamic* film pressures from many cycles of journal motion reveals a zone of uniform low pressure (*gaseous cavitation)* with a magnitude equal to the damper discharge pressure, independently of the air content. The *uniform pressure* zone extends as the air volume fraction increases and develops around the position of local maximum film thickness. The damper forces, peak-to-peak film pressures and drive power decrease as the air content in the bubbly fluid raises, thus evidencing a notable reduction in the damping capability of the *SFD*.

Numerical predictions for the pressure field and fluid film forces for the test *SFD* are presented in Figures 9 through 14. Figure 9 shows the pressure distribution of the bubbly lubricant at $z_2 = 16.7$mm versus the circumferential coordinate θ [1] and corresponding to the different test conditions listed in Table 2. The calculated hydrodynamic pressure fields decrease as the air volume fraction (α_i) increases. The test results also evidence this result. However, the characteristic zone of *uniform pressure* appearing in the measurements of the bubbly fluid pressures is not replicated by the predictions (see Figure 4 for the experimental results). The model predictions show the film pressures to vary gradually without dramatic changes or variations.

Figure 10 provides a comparison of the predicted and test-averaged *peak-to-peak (p-p)* pressures versus the inlet gas volume fraction at the axial locations of measurement, $z_1 = 5.6$mm and $z_2 = 16.7$mm. The predicted *p-p* pressures drop in a more linear form

[1] Note that the dynamic pressure fields shown in Figure 4 depict the pressure versus time at a fixed angular location. The relationship between both coordinate systems is given by $\theta=\theta_s - \omega t$, where θ_s is the fixed angular position.

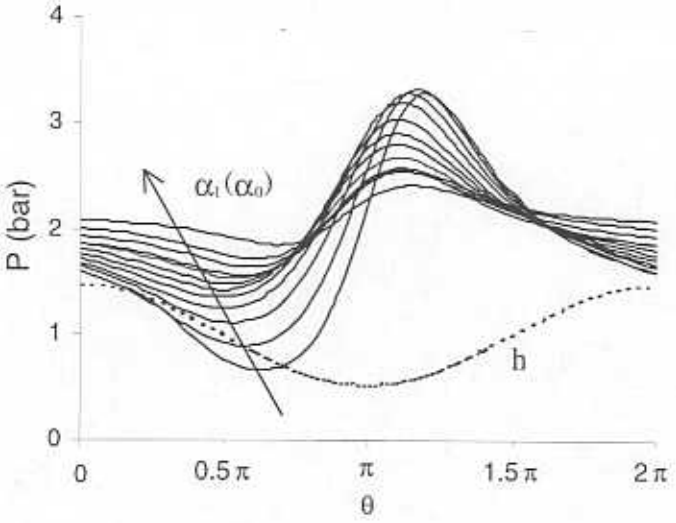

Figure 9: Calculated SFD pressure fields at axial location $z_2 = 16.7\text{mm}$. Effect of gas volume fraction.

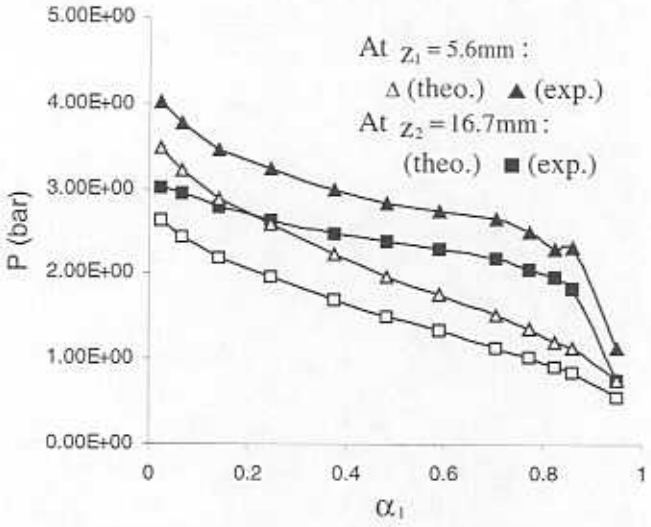

Figure 10: Predicted and test peak-to-peak squeeze film pressures for test SFD versus air volume fraction at axial locations of measurements. Tests at at ω=8.33 Hz.

and more rapidly than the experimental measurements. The large difference, nearly 1 bar, between the underpredictions and the measurements denotes that low values of the air volume fraction (α) do not have a pronounced effect on the generation of squeeze film pressures. Recall, however, that the measured pressures have a large first-order uncertainty in the *p-p* values since these show significant variations every period of journal motion. The (arithmetic) average of journal orbit radius used in the predictions may also be a source for the discrepancies noted.

The pressure measurements allow the estimation of radial and tangential forces (per unit length) at the two axial locations $z_1 = 5.6\text{mm}$ and $z_2 = 16.7\text{mm}$. The tests confirm that the period averaged pressure field is synchronous with the journal whirl frequency and thus generates invariant forces in a rotating (r,t) coordinate system. Figures 11 and 12 show, the experimental and predicted tangential (f_t) and radial (f_r) forces per unit length acting on the journal surface. The tangential force (f_t) decreases as the volume fraction of air increases consistent with the experiments. The correlation of predicted and test results is better than for the peak pressures. The radial force (f_r) differs largely from the experimental forces though it has the right order of magnitude. Recall that the radial force in the measurements is due also to a hydrostatic effect due to the pressure supply conditions. This important condition, not accounted for in the model, may explain the large differences with the predicted results.

Figures 13 and 14 show the predicted *SFD* radial force (F_r) and tangential force (F_t) versus the air volume content. These forces are the result of the integration of the whole pressure field over the journal surface. The tangential force, also known as the damping force, decreases as the air content increases denoting a degradation of the SFD force performance. The force reduction rate is more pronounced for the very small ($\alpha \to 0$) and very large ($\alpha \to 1$) air volume fractions. The radial force increases sharply for small

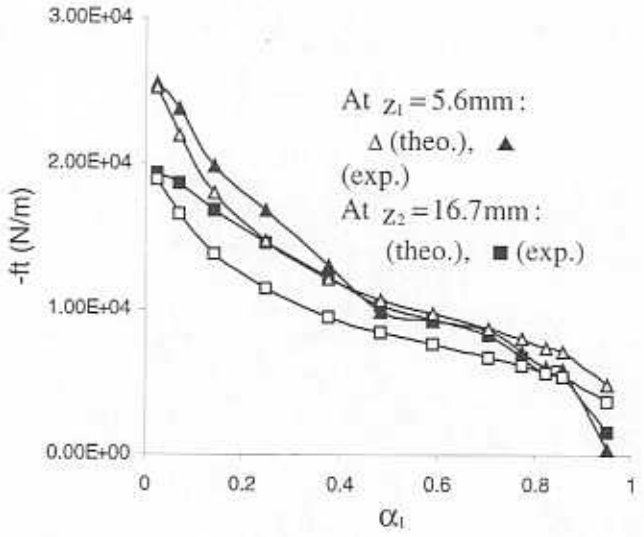

Figure 11: Predicted and test SFD tangential film forces versus air volume fraction at axial locations of measurements. Operation at ω=8.33 Hz.

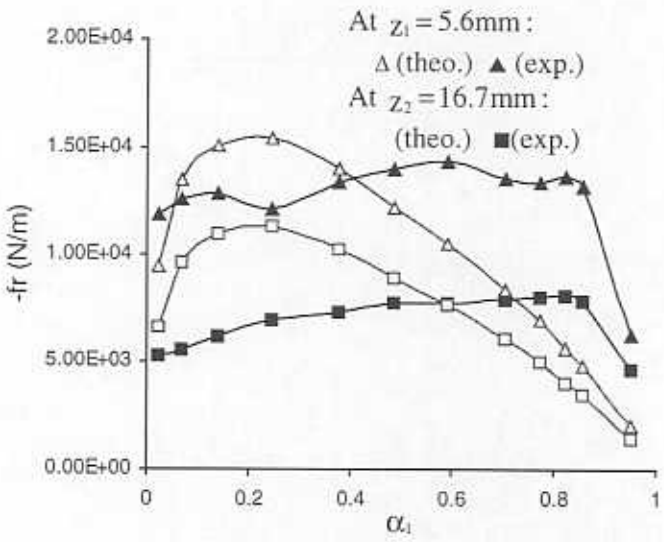

Figure 12: Predicted and test radial SFD film forces versus air volume fraction at axial locations of measurements. Operation at ω=8.33 Hz.

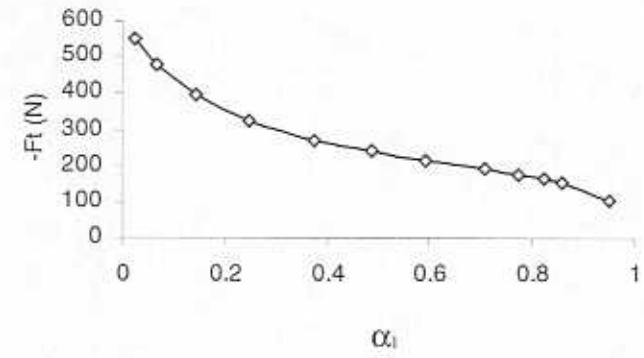

Figure 13. Predicted SFD tangential force versus air volume fraction for operation at ω=8.33 Hz

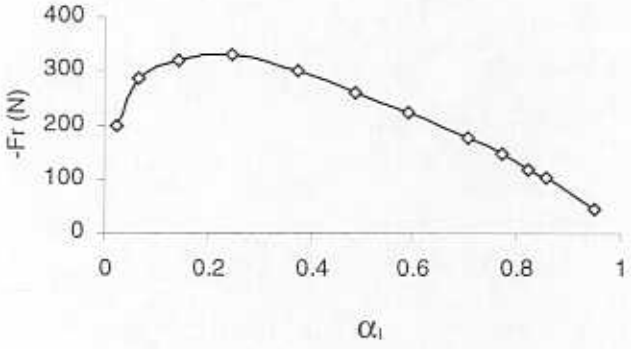

Figure 14: Predicted SFD radial film force versus air volume fraction for operation at ω=8.33 Hz

contents of air, peaks at about 20% of air volume fraction, and then decreases rapidly. Recall that for the pure lubricant case, (α=0), only tangential (damping) forces should appear in a *SFD* without lubricant vaporization or no release of dissolved gases.

Recommendations for Further Work

A continuum based model for the mean motion of a bubbly fluid in a *SFD* has been developed. The model assumes an isothermal process for an incompressible lubricant and an ideal gas moving with identical speeds. Furthermore, the pressure of the lubricant and gas are considered identical in the absence of surface tension effects. The analysis leads to a Reynolds-like thin film lubrication equation for the prediction of the pressure field in the flow region. The air volume fraction and bubbly fluid pressure are related by an

algebraic equation that denotes invariant mass fractions for the gas and lubricant in the flow region. The pressure field is uniquely determined by the air volume fraction at the discharge sides of the damper.

In general, the predicted results for forces agree favorably with the measurements and demonstrate the dramatic reduction in damping (tangential) force as the amount of air in the bubbly lubricant increases. Most notably, a centering radial force providing a stiffness like effect, appears as a consequence of the air entrained within the bubbly lubricant. The discrepancies found may be due to the relation for effective viscosity used in the model, i.e. $\mu=(1-\alpha^4)^{1/2}\ \mu_{LR}$. It is unknown if this relationship is applicable to other *SFD* configurations or for other operating conditions.

Suggested recommendations for further work include:

a) To optimize the relation for the effective viscosity of the bubbly lubricant and based on more detailed comparisons between predicted pressures and available measured pressures. It is important to study the physical significance of this relationship and its applicability to actual damper applications. The effects of surface tension in the bubbles should also be researched with some detail.

b) A more detailed model of the squeeze flow of a bubbly lubricant in thin film regions should include the phenomenon of lubricant cavitation, i.e. oil vaporization or release of dissolved gases. This study requires of a more general formulation where the gas and lubricant (liquid and vapor) mass fractions vary within the flow region. Experimental measurements indicate that for larger whirl frequencies both air entrainment and lubricant vaporization coexist.

c) A physical model that provides a sound relationship for the air volume fraction ingested within the SFD is needed to advance the model and provide a computational predictive tool of practical value. Note that in an actual SFD application the amount of air ingested and entrapped within the damper must depend on the film clearance, the journal whirl frequency and the level of external pressurization to the damper.

d) The current numerical procedure for solution of the governing equation should be enhanced to a block or line-solver to reduce substantially the computing time and to provide a predictive tool of practical use.

e) Further experimental measurements of squeeze film pressures, forces and flow visualizations of the bubbly flow field in a *SFD* should be conducted to verify or modify some of the model assumptions. The test program should also aim to characterize the force performance of *SFD*s at high frequencies and large orbital journal motions.

REFERENCES

Bowen, R. M., 1976, "Theory of Mixtures," in *Continuum Mechanics III*, (A. C. Eringen, ed.), Academic Press, N.Y.

Brewe, D.E., Ball, J.H., and Khonsari, M.M., 1990, editors, "Current Research in Cavitating Fluid Films", *STLE Special Publication SP-28*.

Childs, D., 1993, "Turbomachinery Rotordynamics," John Wiley & Sons, New York.

Diaz, S., and San Andres, L., 1997, "Forced Response of a Squeeze Film Damper Operating with a Bubbly (Air/Oil) Mixture," TAMU Turbomachinery Research Consortium Report, TRC-*SFD*-1-97, April.

Diaz, S., and San Andrés, L., 1998a, "Reduction of the Dynamic Load Capacity in a Squeeze Film Damper Operating with a Bubbly Lubricant," *ASME Turbo Expo'98* Conference, Stockholm, Sweden, June.

Diaz, S., and San Andrés, L., 1998b, "Effects of Bubbly Flow on the Dynamic Pressure Fields of a Test Squeeze Film Damper," *(FEDSM'98) 1998 ASME Fluids Engineering Division Summer Meeting*, Washington, DC, June.

Dowson, D., Godet, M., and Taylor, C.M., 1974, editors, "Cavitation and Related Phenomena in Lubrication", ImechE, England.

San Andrés, L., and J.M. Vance, 1986, ""Effects of Fluid Inertia and Turbulence on the Force Coefficients for Squeeze Film Dampers," ASME *Journal of Engineering for Gas Turbines and Power*, Vol. 108, pp. 332-339.

Rajagopal, K. R., and Tao, L., 1995, "Mechanics of Mixtures," Series on Advances in Mathematics for Applied Sciences, Vol. 35, World Scientific, Singapore.

Zeidan, F., San Andrés, L., and Vance, J.M., 1996, "Design and Application of Squeeze Film Dampers in Rotating Machinery," Proc. of the 25^{th} *Turbomachinery Symposium*, Texas A&M University, September, pp. 169-188.

APPENDIX A
DETAILS OF FLOW ANALYSIS

Neglecting the fluid inertia terms and substituting the dimensionless quantities defined in eqns. (20) into eqns. (10-14), renders the following dimensionless equations

$$\frac{\partial}{\partial\theta}(\bar{\rho}_G\bar{u}_\theta)+\frac{\partial}{\partial\bar{y}}(\bar{\rho}_G\bar{u}_y)+\frac{R}{L}\frac{\partial}{\partial\bar{z}}(\bar{\rho}_G\bar{u}_z)=0, \tag{A.1}$$

$$\frac{\partial}{\partial\theta}((1-\alpha)\bar{u}_\theta)+\frac{\partial}{\partial\bar{y}}((1-\alpha)\bar{u}_y)+\frac{R}{L}\frac{\partial}{\partial\bar{z}}((1-\alpha)\bar{u}_z)=0, \tag{A.2}$$

$$\left(\frac{R}{c}\right)^2\frac{\partial}{\partial\bar{y}}\left(\bar{\mu}\frac{\partial\bar{u}_\theta}{\partial\bar{y}}\right)+2\frac{\partial}{\partial\theta}\left(\bar{\mu}\frac{\partial\bar{u}_\theta}{\partial\theta}\right)+\frac{\partial}{\partial\bar{y}}\left(\bar{\mu}\frac{\partial\bar{u}_y}{\partial\theta}\right)+\frac{R}{L}\frac{\partial}{\partial\bar{z}}\left(\bar{\mu}\frac{\partial\bar{u}_z}{\partial\theta}\right)+\left(\frac{R}{L}\right)^2\frac{\partial}{\partial\bar{z}}\left(\bar{\mu}\frac{\partial\bar{u}_\theta}{\partial\bar{z}}\right)=\frac{P_0}{\omega\mu_{LR}}\frac{\partial\bar{P}}{\partial\theta}, \tag{A.3}$$

$$2\frac{\partial}{\partial\bar{y}}\left(\bar{\mu}\frac{\partial\bar{u}_y}{\partial\bar{y}}\right)+\frac{\partial}{\partial\theta}\left[\bar{\mu}\left(\left(\frac{c}{R}\right)^2\frac{\partial\bar{u}_y}{\partial\theta}+\frac{\partial\bar{u}_\theta}{\partial\bar{y}}\right)\right]+\frac{R}{L}\frac{\partial}{\partial\bar{z}}\left[\bar{\mu}\left(\frac{\partial\bar{u}_z}{\partial\bar{y}}+\frac{R}{L}\frac{\partial\bar{u}_y}{\partial\bar{z}}\right)\right]=\frac{P_0}{\omega\mu_{LR}}\frac{\partial\bar{P}}{\partial\bar{y}}, \tag{A.4}$$

$$\left(\frac{R}{c}\right)^2\frac{L}{R}\frac{\partial}{\partial\bar{y}}\left(\bar{\mu}\frac{\partial\bar{u}_z}{\partial\bar{y}}\right)+\frac{L}{R}\frac{\partial}{\partial\theta}\left[\bar{\mu}\left(\frac{\partial\bar{u}_z}{\partial\theta}+\frac{R}{L}\frac{\partial\bar{u}_\theta}{\partial\bar{z}}\right)\right]+\frac{\partial}{\partial\bar{y}}\left(\bar{\mu}\frac{\partial\bar{u}_y}{\partial\bar{z}}\right)+2\frac{R}{L}\frac{\partial}{\partial\bar{z}}\left(\bar{\mu}\frac{\partial\bar{u}_z}{\partial\bar{z}}\right)=\frac{P_0}{\omega\mu_{LR}}\frac{\partial\bar{P}}{\partial\bar{z}}. \tag{A.5}$$

The order of magnitude of θ, $\bar{y}$, $\bar{z}$, $\bar{\rho}_G$, α, $\bar{\mu}$ and R/L is one (unit value). Based on (A.1), (A.2) and the flow conditions prevailing in a typical SFD, it is customary to assume that $\bar{u}_\theta$, $\bar{u}_y$ and $\bar{u}_z$ are also of order of magnitude one. Thus, the terms not related to $(R/c)^2$ on the left-hand side of (A.3), (A.4) and (A.5) can be neglected since $R/c >> 1$, and then eqns. (A.3), (A.4) and (A.5) reduce to

$$\left(\frac{R}{c}\right)^2\frac{\partial}{\partial\bar{y}}\left(\bar{\mu}\frac{\partial\bar{u}_\theta}{\partial\bar{y}}\right)=\frac{P_0}{\omega\mu_{LR}}\frac{\partial\bar{P}}{\partial\theta}, \tag{A.6}$$

$$\frac{\partial\bar{P}}{\partial\bar{y}}=0, \tag{A.7}$$

$$\left(\frac{R}{c}\right)^2\frac{L}{R}\frac{\partial}{\partial\bar{y}}\left(\bar{\mu}\frac{\partial\bar{u}_z}{\partial\bar{y}}\right)=\frac{P_0}{\omega\mu_{LR}}\frac{\partial\bar{P}}{\partial\bar{z}}. \tag{A.8}$$

The size of the bubbles is large relative to the radial clearance of the damper, which implies that the gas volume fraction (α) is independent of the cross-film coordinate y (or $\bar{y}$), and so is $\bar{\rho}_G$ from eqns. (A.7) and (7).